SOILS AND FOUNDATIONS Vol. 40, No. 2, 9-20, Apr. 2000 Japanese Geotechnical Society

SOIL DENSIFICATION DUE TO STATIC SAND PILE INSTALLATION FOR LIQUEFACTION REMEDIATION

YOSHIMICHI TSUKAMOTOⁱ⁾, KENJI ISHIHARAⁱⁱ⁾, MINORU YAMAMOTOⁱⁱⁱ⁾, KENJI HARADAⁱⁱⁱ⁾ and HIROSHI YABE^{iv)}

ABSTRACT

Among various soil densification techniques, the sand compaction pile (SCP) has been one of the most frequently used methods to improve loose deposits of sandy soils encountered in Holocene or reclaimed lands. In this method, columns of densely compacted sand are created in the ground by imparting vibration to the sand at the bottom of a pipe which is lifted stepwise while supplying sand from the ground surface. Because of noise and vibration produced during its installation, the SCP is losing its popularity and an alternative technique employing a static driving force is being exploited to install columns of dense sand. To study the degree of soil densification due to such static sand pile installation, multiple series of large-scale hollow cylindrical torsional shear tests were conducted in the laboratory on clean fine sand, simulating stress changes conceived to be occurring in a soil element in the vicinity of the pile being penetrated. To determine the stress changes in the field during the pile penetration, analysis was conducted based on the classical theory of elasticity. The sequence of stress changes thus established was applied to saturated sand specimens prepared in a torsional hollow cylindrical shear test apparatus. This process allows complex stress paths to be reproduced in the specimens, including the rotation of a principal stress direction. In the course of the tests, shear stresses were applied first undrained on loose and medium dense fine sands and induced pore water pressure was dissipated by opening the valve of the drainage system, thereby monitoring the volume decrease of saturated samples. Particular attention was drawn to the influence of the amount of shear strains imposed undrained on the soil specimens on the subsequent drained volume changes. It was found that a volume change of $5 \sim 10\%$ was observed in the test samples, which is considered sufficiently great to bring about substantial densification in the sand. The experimental results of the tests were shown to provide a basis for the assessment of soil densification due to static sand pile penetration. On this basis, a diagram was provided to facilitate the evaluation of the degree of soil densification. In addition, case studies were carried out by taking advantage of soil improvement projects which have recently been implemented at three sites in Japan. These are considered to provide field verification on the effectiveness of soil densification due to static sand pile installation. Finally the degree of in-situ densification as evidenced by increased SPT N-value was interpreted in the framework of the conception established through the laboratory tests.

Key words: density, drainage, pile driving, sand compaction pile, static (IGC: D9/K7)

INTRODUCTION

A sand compaction pile (SCP) method is frequently used to densify sandy soil deposits and to improve their capability to resist liquefaction during earthquakes, (Kusano, 1983; Mizuno et al., 1987; JSSMFE, 1978; PHRI, 1997 and others). The installation of sand compaction piles consists of a sequence of routine work, as illustrated in Fig. 1. First, the casing pipe is penetrated forcibly into the ground to a specified depth by employing vibration with a frequency of 50 Hz. Then, the casing pipe is retracted stepwise, each time about 1 metre. Simul-

taneously, the sand is supplied from the ground surface through the casing pipe, and compacted by its tip, while applying vertical vibration. The lower end of the casing pipe is controlled to open while the pipe is lifted and closed when compacting the sand below it. This sequence of sand supply and compaction is repeated many times until a compacted column of sand is fully formed through the specified depth. Dozens of sand compaction piles are normally installed at a site with an equal spacing to cover the area of soil improvement. It is recognized that in this technique actual penetration is advanced by the force pushing the pile and vibration is merely to help

¹⁾ Lecturer, Department of Civil Engineering, Science University of Tokyo, 2641, Yamazaki, Noda City, Chiba 278-8510.

ii) Professor, ditto.

Soil Engineering Division, Fudo Construction Co., Ltd.

Fudo Construction Co., Ltd. (Formerly graduate student, Department of Civil Engineering, Science University of Tokyo.)
Manuscript was received for review on July 23, 1998.

Written discussions on this paper should be submitted before November 1, 2000 to the Japanese Geotechnical Society, Sugayama Bldg. 4F, Kanda Awaji-cho 2-23, Chiyoda-ku, Tokyo 101-0063, Japan. Upon request the closing date may be extended one month.

10 TSUKAMOTO ET AL.

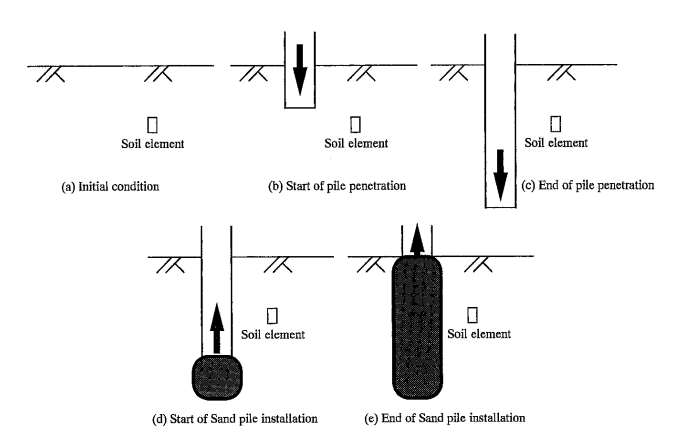


Fig. 1. Installation of sand compaction piles

penetration by cutting the friction over the outside walls of the pipe. However, because of environmental problems such as noise and vibration cropping up in recent years particularly in densely populated areas, the use of vibration-type techniques is often restricted, and the technique of static compaction is preferred to those of dynamic force. Under such circumstances, a soil densification technique by means of static pile penetration has been developed by the private sector, and elaborated into practice in recent years, (PHRI, 1997). In this technique, the rotating casing pipe is gradually pushed into the ground without any application of vertical vibration. Then the same sequence of sand supply and compaction as the sand compaction pile method is repeated during the pullout of the casing pipe, until the compacted sand column is installed. It has been observed in the field that compacted sand columns installed by static technique gave rise to an increase in SPT N-value of about 10 for loose deposits of sand having an N-value of about 10. This increase in the SPT N value was shown to correspond to 30% increase in the relative density calculated by the empirical relation of $D_r(\%) = 21 \sqrt{N/(\sigma_v + 0.7)}$, $(\sigma_v: \text{kgf/cm}^2)$, (Meyerhof, 1957). Therefore, the soil improvement by means of the statically compacted sand pile has proved to be effective in densifying sand deposits.

The occurrence of soil densification in the course of compaction pile installation may be envisioned as a superposition of two working mechanisms as follows. First, all of the soils displaced by the volume of the pile are pushed outwards into the surrounding soil deposit and impose shear distortion upon it, while the displaced soil itself is subjected to shear distortion. The density increase due to this effect may be noticeable, although the ground surface tends to heave and may compensate for part of the volume change. The second aspect of sand pile driving is that the soil element in the vicinity of the compaction pile experiences a series of stress changes due to the vertical load applied at the bottom of the casing pipe during penetration and retraction. These stress changes may be induced in undrained conditions with a fairly large amount of shear strain and when the induced positive pore water pressure is dissipated, soil densification can take place. The second working hypothesis as cited above

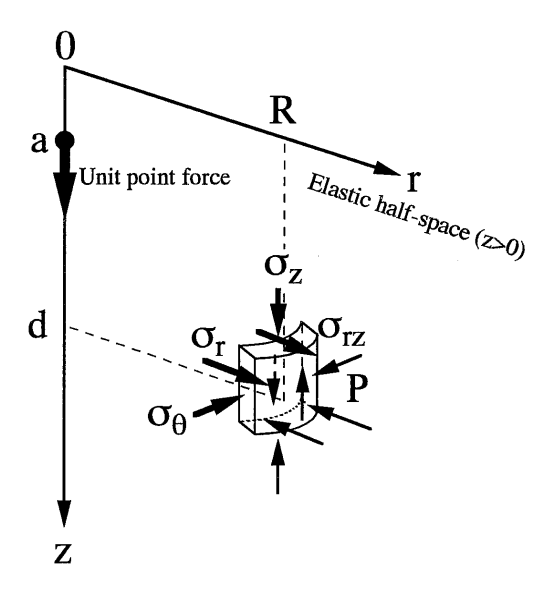


Fig. 2. Scheme of analysis of field stress path due to pile driving

is the major point to be addressed and clarified in this paper.

FIELD STRESS PATH

Actual stress paths to which a soil element in the ground might be subjected during sand pile penetration would be complex, but the use of elastic analyses could provide the overall feature of stress changes that may occur in the ground in which a vertical point force is considered to travel in the vertical direction from the surface to the depth of pile penetration. It is well known that the Boussinesq's solution is known to give stress distributions as functions of Poisson's ratio v, and it is only when strains are concerned that the shear modulus G must be specified and incorporated in the formula. This implies that stresses are relatively insensitive to the changes in the material constants, compared with the deformations or strains evaluated by virtue of the elastic theory. Therefore, it would be appropriate to assume that the theory of elasticity offers, with a reasonable degree of accuracy, an estimate of stresses induced in the interior of a half space such as level ground.

In the following, a field stress path to which a soil element is subjected in the vicinity of sand pile penetration is analysed, assuming a single vertical point force moving downward in the interior of an elastic half space (semi-infinite solid). The elastic solution for the axi-symmetric problem as above was given in the references by Mindlin (1936) and Mogami (1957). In what follows, the expressions derived by Mogami (1957) are adopted. Figure 2 shows polar coordinates (z, r) adopted in this analysis, and stress components acting on the soil element. The states of stress $(\sigma_r, \sigma_z, \sigma_{rz}, \sigma_\theta)$ at point P located at (d, R), (d=1, unit depth), due to the unit force acting at (a, 0), can be calculated by the formulae. The field stress path can be obtained by assuming that the unit force moves successively from the origin to some depth along the z-

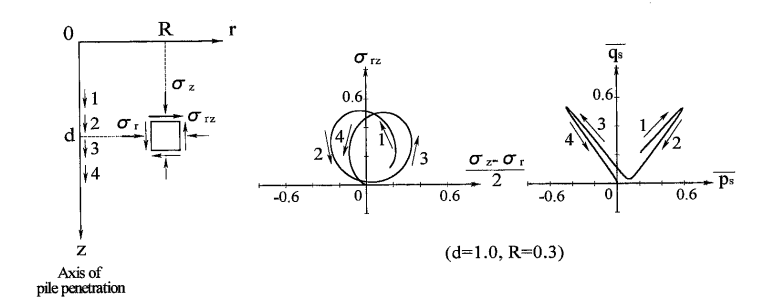


Fig. 3. Field stress path

axis. The details of the calculation of the field stress path are described in the Appendix. Based on the calculation of the field stress path thus obtained, it is found that the stress component σ_{θ} does not change significantly; the ratios of the normal stresses, $|\sigma_{\theta}/\sigma_z|$ and $|\sigma_{\theta}/\sigma_r|$, are found to vary within the ranges of 3% and 27%, respectively, while $|\sigma_{\theta}/\sigma_{rz}|$ varies within 10%. Therefore, the stress components of major interest for the problem of sand pile penetration are certainly σ_r , σ_z , σ_{rz} that are induced on the z-r plane. Figure 3 shows two diagrams, $((\sigma_z-\sigma_r)/2, \sigma_{rz})$ and (\bar{p}_s, \bar{q}_s) , tracing the field stress path for R=0.3 which is calculated by the above method, where

$$\bar{p}_s = \frac{\sigma_z + \sigma_r}{2},$$

$$\bar{q}_s = \sqrt{\left(\frac{\sigma_z - \sigma_r}{2}\right)^2 + \sigma_{rz}^2}.$$
(1)

In this diagram, the soil element is subject to the elliptical stress path orientated towards left on the $(\sigma_z - \sigma_r)/2 - \sigma_{rz}$ plane and the mean stress \bar{p}_s increases, until the unit force advances from the origin to the depth at which the soil element P is located. After the unit force passes through it, the soil element is subject to the elliptical stress path orientated towards the right on the $(\sigma_z - \sigma_r)/2 - \sigma_{rz}$ plane and the mean stress \bar{p}_s is reduced. It is interesting to note that the direction of principal stresses gradually rotates and the shear stress component σ_{rz} only takes positive values as indicated by the stress path being located in the upper half of the stress space. To simulate the stress changes due to static sand pile penetration in the experiments reported below, the above calculated field stress paths are used. However, for the pullout procedure during the sand pile installation, it is assumed that the stress changes occur in a reverse manner to the above calculated field stress paths. Therefore, to simulate the entire sequence of one sand pile penetration and pullout, the above field stress paths are first applied and then are applied again but in a reverse manner. Furthermore, to simulate the stress changes that occur in the soil element in between the two adjacent sand compaction piles, the above field stress paths are first applied, and then the same field stress paths are applied again except in a negative direction with respect to the shear stress σ_{rz} .

It would be of interest to examine actual values of

stress changes encountered in the field. The maximum vertical load generated at the bottom of the casing pipe during static sand compaction pile installation is known to be about 450 kN, (Fudo Construction, 1996). Thus, the maximum deviator stress \bar{q}_s induced for instance at a place 5 metres deep and 1 metre away from the pile axis is estimated to be about 20 kPa. At a closer point 0.5 metres away at the same depth, \bar{q}_s is estimated as 80 kPa. The maximum deviator stress induced at a soil element closer to the pile axis than the points considered above certainly becomes greater.

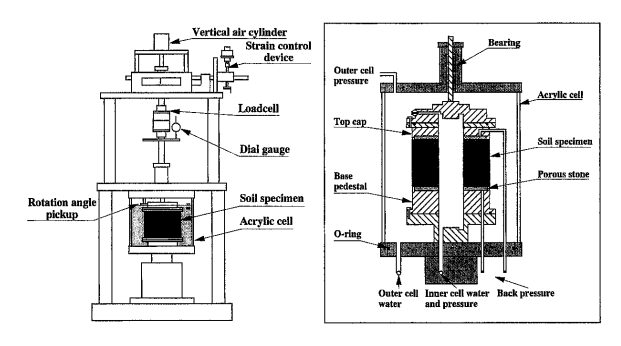
EXPERIMENTAL APPARATUS

To duplicate the above-mentioned stress changes in specimens in the laboratory, a large-scale hollow cylinder apparatus is used in this study. The dimensions of the hollow cylindrical specimen are approximately 140 mm in height, 250 mm in outer radius, and 150 mm in inner radius. One of the advantages of using the hollow cylindrical test apparatus lies in the fact that complex stress paths including the rotation of a principal stress direction can be reproduced in the specimens. Figure 4 shows the hollow cylinder apparatus used for this study and the hollow cylindrical specimen, illustrating external forces, stresses and strains that can be achieved on the specimen. The vertical load V, torque T, and inner and outer cell pressures P_i and P_o , can be independently controlled, through which the four components of stresses, σ_z , σ_r , σ_θ and $\sigma_{z\theta}$, are induced. In the tests described below, the torque T was applied by a motor-driven device in a straincontrolled manner, and the other components of the vertical force V, and the inner and outer pressures P_i and P_o were controlled to follow a stress path specified for conduct of each test. The pore water pressure u could also be measured in undrained tests. Among these stresses, the normal stress σ_r is in itself a principal stress, and the plane stress condition is considered to be produced when the principal stress σ_r is kept constant. The other two principal stresses are produced by a combination of σ_z , σ_{θ} and $\sigma_{z\theta}$, and the direction of a major principal stress α is defined as follows,

$$\tan 2\alpha = \frac{2\sigma_{z\theta}}{\sigma_z - \sigma_\theta}.$$
 (2)

The measurement of the deformation of the soil speci-

12 TSUKAMOTO ET AL.



(a) Test apparatus

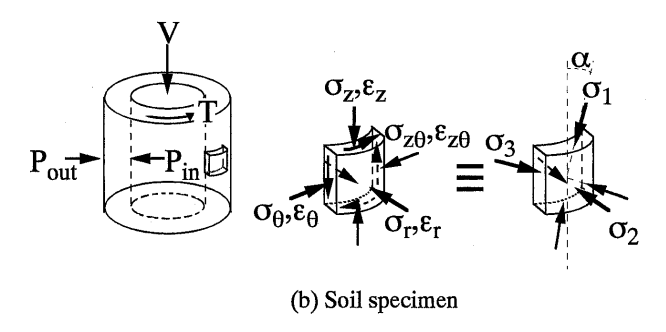


Fig. 4. Hollow cylindrical torsional shear tests: (a) Test apparatus, (b) Soil specimen

Table 1. Physical properties of Toyoura sand

Specific gravity G_s	2.65
Mean diameter D_{50} (mm)	0.19
Uniformity coefficient U_c	1.70
Maximum void ratio e_{max}	0.988
Minimum void ratio e_{\min}	0.616

men was made for the vertical displacement v, rotation angle θ , inner cell volume change ΔV_i , and specimen volume change ΔV_s , through which the four components of strains, ε_z , ε_r , ε_θ and $\varepsilon_{z\theta}$, and therefore the principal strain components, ε_1 , ε_2 and ε_3 , are calculated. The resulting volumetric and deviatoric strains, ε_v and γ , are defined, respectively, as follows,

$$\varepsilon_{v} = \frac{\Delta V_{s}}{V_{si}} = \varepsilon_{1} + \varepsilon_{2} + \varepsilon_{3},$$

$$\gamma = \sqrt{\frac{2}{9} \left\{ (\varepsilon_{1} - \varepsilon_{2})^{2} + (\varepsilon_{2} - \varepsilon_{3})^{2} + (\varepsilon_{3} - \varepsilon_{1})^{2} \right\}},$$
(3)

where V_{si} is the initial volume of the soil specimen.

The saturated sand called "Toyoura sand" is used in the tests. This sand, consisting of quartz-based particles has been widely used in Japan, and has grain characteristics as shown in Table 1.

STRESS PATH APPROACH

When the principal stress σ_r is kept constant in the hollow cylinder apparatus, a plane stress condition is achieved on the z- θ plane. Under this condition, the two-dimensional mean stress \bar{p} or \bar{p}' , and deviator stress \bar{q} , can be defined as follows,

$$\bar{p} = \frac{\sigma_z + \sigma_\theta}{2}, \quad \bar{p}' = \frac{\sigma_z + \sigma_\theta}{2} - u,$$

$$\bar{q} = \sqrt{\left(\frac{\sigma_z - \sigma_\theta}{2}\right)^2 + \sigma_{z\theta}^2}.$$
(4)

It can be seen that the field stress path simulation of sand pile penetration on the z-r plane as illustrated in Fig. 2 can be achieved in the samples in the stress changes occurring on the z- θ plane of the hollow cylindrical specimen. In other words, the stress components, σ_r , σ_z , σ_{rz} , representing the stress changes during the sand pile penetration can be replaced by the stresses σ_{θ} , σ_{z} , $\sigma_{z\theta}$ that are induced on the hollow cylindrical specimen. In all of the tests presented below, the specimens were prepared by the method of air pluviation, in which dry sand is discharged vertically in air from a small nozzle into the mould. The specimens were then saturated to satisfy Skempton's B value greater than 0.98 under isotropic consolidation of $\bar{p}' = 20$ kPa. They were finally consolidated isotropically to achieve an effective mean stress of $p' = (\sigma_1' + \sigma_2' + \sigma_3')/3 = 100 \text{ kPa}$ $\bar{p}' = 100 \text{ kPa}$, $\bar{q} = 0 \text{ kPa}$, $\sigma_r' = 100 \text{ kPa}$. After the specimens were properly consolidated, drained or undrained shear loading was implemented. Based on the fact that the stress component σ_{θ} does not change significantly in the calculated field stress path as mentioned above, the principal stress σ_r , which is the counterpart of the above calculated stress component σ_{θ} in the experiments, was kept constant during drained or undrained shear loading and unloading in all the test series. It is to be noted that the coefficient of the intermediate principal stress $b = (\sigma_1 - \sigma_2)/(\sigma_1 - \sigma_3)$ =0.5 was maintained throughout the shear loading and unloading processes, where the principal stress σ_r was maintained constant.

DRAINED RESPONSE SUBJECT TO FIELD STRESS PATH

Test Procedure

In order to examine the drained behaviour of soils undergoing stress changes during sand pile penetration, drained shear tests were carried out. The actual stress paths followed by these drained shear tests are illustrated in Fig. 5. Since these stress paths are based on the calculated field stress path where Poisson's ratio v is assumed to be 0.5, the direct application of these field stress paths to drained shear tests may be impaired. However, for comparison purposes, the same field stress paths were applied to drained as well as undrained shear tests described below. In the drained shear tests, the stress path consists of four cycles of shear loading and unloading. The specimens were first sheared along the elliptical stress path orientated towards top-left on the $(\sigma_z - \sigma_\theta)/2 - \sigma_{z\theta}$ plane, while the mean effective stress \bar{p}' was increased or decreased together with the shear stress \bar{q} . The elliptical stress path orientated towards top-right on the $(\sigma_z - \sigma_\theta)$ / $2-\sigma_{z\theta}$ plane was then followed, while the mean effective stress \bar{p}' was reduced or increased together with the shear stress. The field stress path achieved thus far in the test is

deemed to duplicate the stress changes which occur during penetration of one single pile. However, when another pile is penetrated at a place opposite to the first pile, the soil element is considered to undergo another sequence of the field stress path, as illustrated in Fig. 5. Therefore, another sequence of the same field stress path with the negative shear stress $\sigma_{z\theta}$ may need to be applied to the specimen, as shown in Fig. 5. Thus, notation of $\bar{q}_{(+)}$ and $\bar{q}_{(-)}$ are introduced to distinguish the values of \bar{q} between these two cases.

Test Results

Two series of tests were conducted with different magnitudes of the maximum shear stress $\sigma_{z\theta}$ of 20 and 30 kPa. The specimens were consolidated to achieve a void ratio of $e=0.86\sim0.88$, which corresponds to the relative density of $D_r=25\sim30\%$. Figure 6 shows the test results with the maximum shear stress of $\sigma_{z\theta}=30$ kPa. It can be seen that the test was conducted so as to exactly follow specified field stress paths, and the void ratio changes during drained shear loading and unloading are also shown in this diagram in which e_0 is the initial void ratio, and e_N

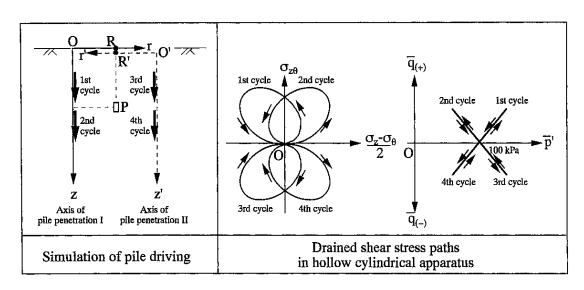
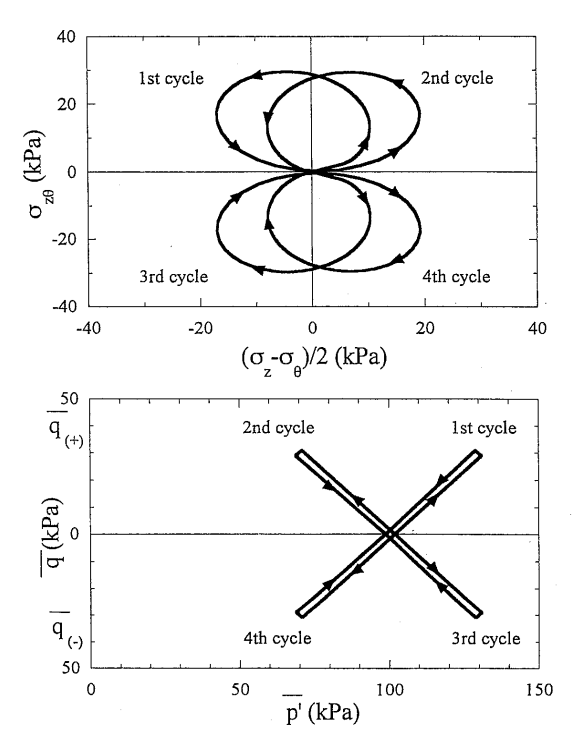


Fig. 5. Drained shear stress paths



 $(N=1\sim4)$ is the void ratio observed after the Nth cycle of drained shear stress application. It should be noted here that the mean stress \bar{p}' is reduced and critically approaches the effective stress failure envelope in the 2nd and 4th cycles, and subsequently the deviatoric strain γ rapidly increases. It is a characteristic of drained shear tests in which the shear stress greater than a certain value cannot be sustained when they reach the failure envelope on the \bar{p}' - \bar{q} plane, whereas in the case of the undrained tests, stress paths can move along the failure envelope and the shear stress can consequently increase or decrease when they reach the failure envelope. It can be seen in this diagram that the deviatoric strain γ achieved in the drained tests are of the order of less than 1.4%, and the void ratio changes due to drained shear paths are generally very small, corresponding to a relative density increase of 5% at most. Such small changes in density cannot account for the substantially larger changes in density observed in the field. Thus, it can be mentioned that the simulations of in-situ stress changes are not appropriate if they are assumed to occur in drained conditions.

UNDRAINED RESPONSE SUBJECT TO VARIOUS STRESS PATHS

Test Procedure

The in-situ condition in the soil elements adjacent to sand pile penetration may be neither completely drained nor undrained; it may be in a partially drained condition. Drained behaviour of fine sand was examined in the above section. To see the influence of pore water generation on the undrained behaviour of soil subject to sand pile driving and the subsequent volume change, multiple

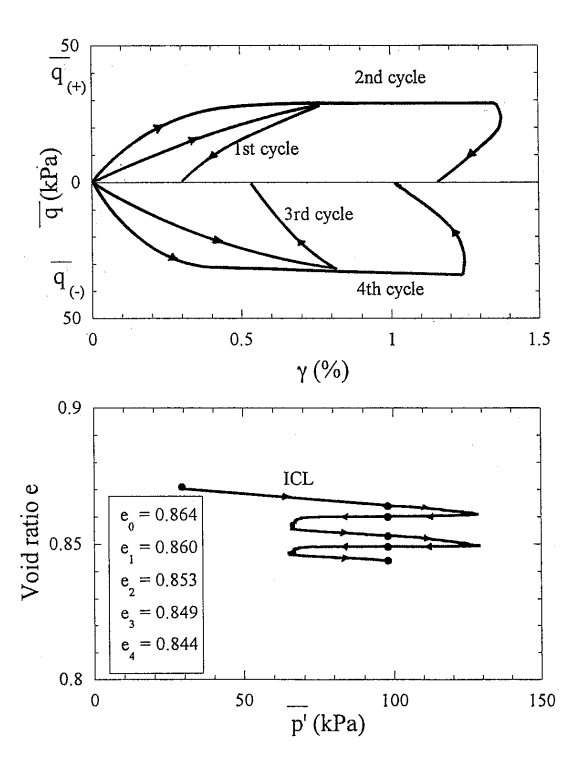


Fig. 6. Drained shear test results

14 TSUKAMOTO ET AL.

series of undrained tests were conducted. To facilitate conduct of the experiments, the following simplified total stress paths were adopted, while appreciating the nature of the calculated field stress paths adopted in the drained shear tests mentioned above. These stress paths are deemed to duplicate those in the field and capture the fundamental aspects of soil behaviour occurring in the field.

Figure 7 shows four series of undrained shear tests carried out in this study. In test series 1, the direction of a major principal stress was fixed at $\alpha = 45^{\circ}$ and the total mean stress \bar{p} was kept constant during cycles of shear stress application. In test series 2, while the total mean stress \bar{p} was always kept constant, the direction of the major principal stress α was changed in all the four cycles of load application shown in Fig. 7. However, α was fixed as $\alpha = 67.5^{\circ}$, 22.5°, -67.5° and -22.5° in the first, second, third and fourth cycles, respectively. In test series 3, during all the four cycles of shear stress application, the direction of a major principal stress was changed in the same manner as in test series 2, but the total mean stress was increased or decreased in the cycles in the same manner as in the case of the drained shear tests illustrated in Fig. 5. Note that the above four cycles correspond to the stress path simulation of loading produced by penetration of two sand piles. To simulate penetration of additional two sand piles, the same four

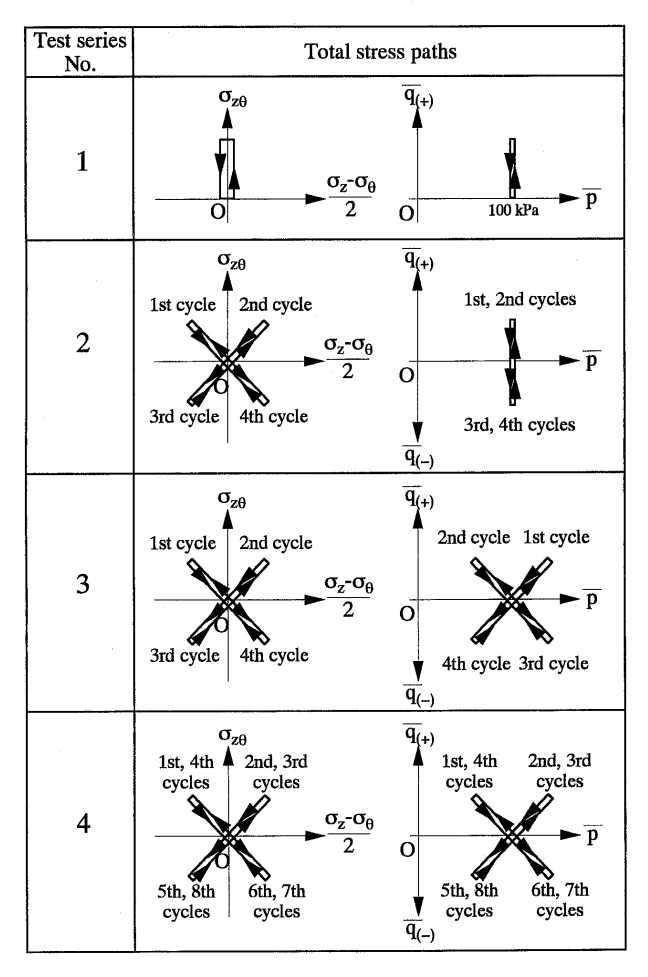


Fig. 7. Undrained shear stress paths

cycles of the stress application as above were repeated in each of the tests.

To be more specific, a specimen was first sheared by a load application following a specified total stress path under an undrained condition until a predetermined maximum shear strain γ_{max} was achieved, and then unloaded. The drainage valve was then opened to let the excess pore water drain out of the specimen, and the amount of volume change was measured. The subsequent cycles of undrained shear loading, unloading and excess pore water drainage were carried out in the same manner.

The influence of shear strain levels at the time of undrained loading on the subsequent volume change was also examined in each of the test series, and at least three tests were performed with different predetermined maximum shear strains of γ_{max} .

Test Results

Figure 8 shows one of the results of test series 1 on loose sand in which the principal stress direction α was kept constant at 45° and the total mean stress \bar{p} was kept constant. In this test, the shear stress was applied until a deviatoric strain of $\gamma = 2.7\%$ was reached in each cycle. It can be seen in the \bar{p}' - \bar{q} diagram that the effective stress path moved along the effective failure envelope. Figure 9 shows one of the results of test series 2 on a loose specimen in which the total mean total stress \bar{p} was kept constant, and the principal stress direction α was maintained at 67.5° , 22.5, -67.5° , and -22.5° in the first, second, third and fourth cycles, respectively. In this test, the shear stress was also applied until the deviatoric strain of 2.7% was reached in each cycle. It is interesting to note here that the effective stress paths in the \bar{p}' - \bar{q} diagram moved along the effective failure envelopes denoted by $\alpha = \pm 22.5^{\circ}$ and $\alpha = \pm 67.5^{\circ}$. On the other hand, Symes et al. (1984) showed the undrained test results of a hollow cylinder apparatus in which the inclination of the effective stress failure envelope on the p'-q plane changed with the angle of principal stress direction α . It is observed in Figs. 8 and 9 that the inclinations of the effective failure envelopes became lower as the principal stress direction α became larger, which is in agreement with the observations made by Symes et al. (1984). It should also be noted here that the maximum deviator stress \bar{q} in the tests presented in Figs. 8 and 9 was within the range of 20 kPa to 80 kPa, which is consistent with the deviator stress estimated by the theory of elasticity described in the above section.

Density Effects

Figure 10(a) summarizes the results of test series 3, where the initial relative density D_{ri} of the soil specimen is plotted against the increase in relative density ΔD_r . In this diagram, it is interesting to see how the increase in the relative density becomes less pronounced as the initial relative density becomes greater. Furthermore, to simulate the process of pile penetration as well as pullout during the installation of sand piles, test series 4 was carried out. In this test series, the stress path simulation of pull-

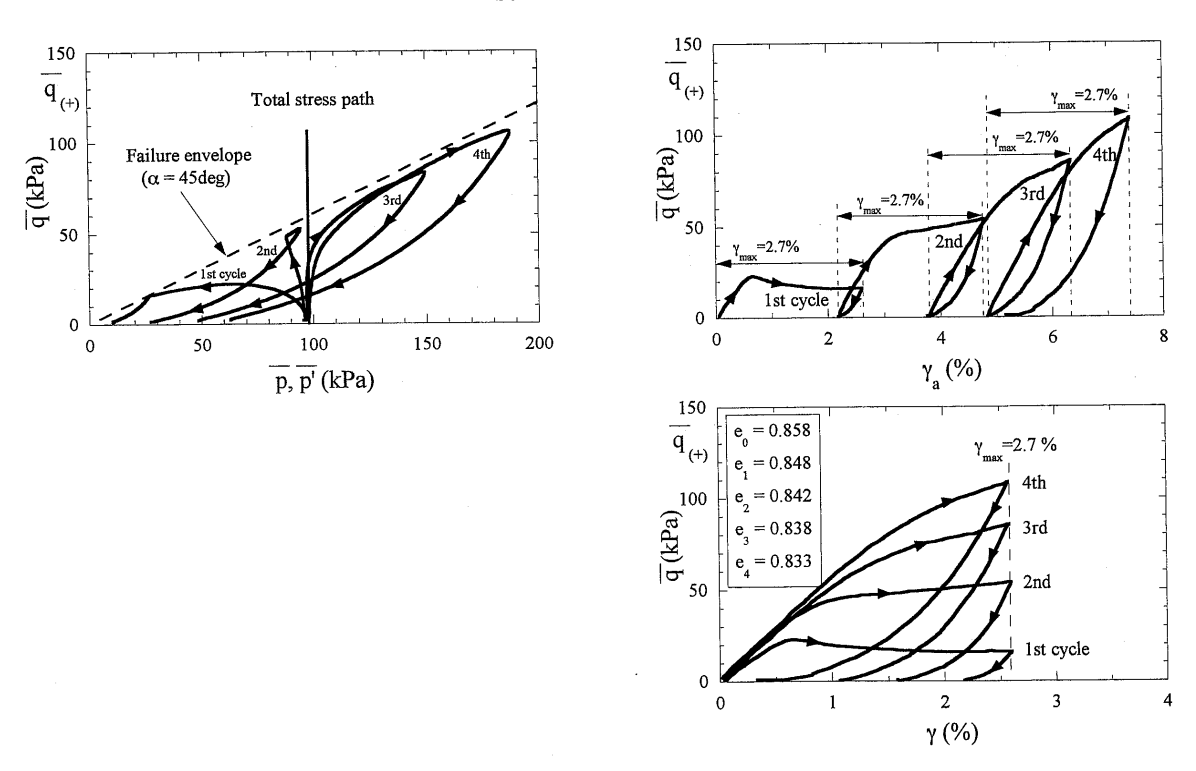


Fig. 8. Undrained shear test results (Test series 1)

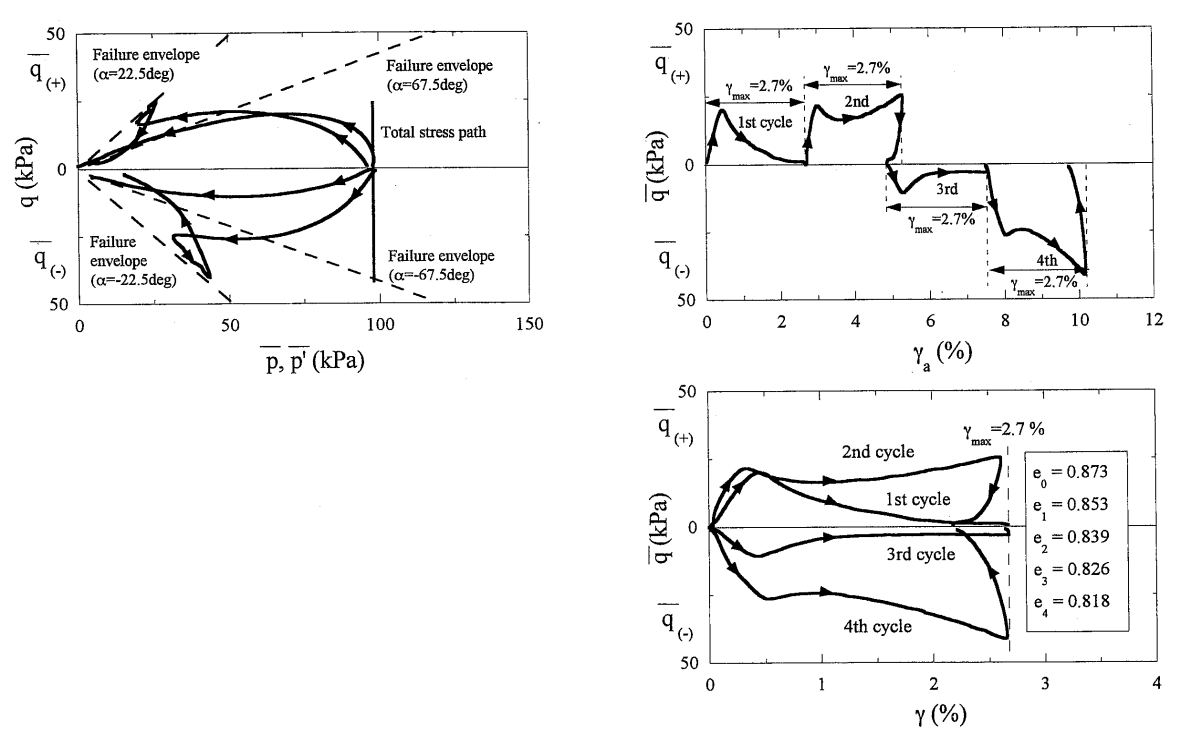


Fig. 9. Undrained shear test results (Test series 2)

out was made by reversing the stress paths of the two cycles corresponding to the pile penetration. The stress path simulation of one sequence of pile penetration and pullout therefore consists of four cycles. To simulate four sequences of pile penetration and pullout, a total of sixteen cycles were applied in this test series. The assumption of the application of sixteen cycles for the simula-

tion of four sequences of pile penetration and pullout may be different from the actual stress changes that occur in the field, since the four sand columns surrounding the particular soil element concerned were installed diagonally. However, it is considered in this study that this influence may be within a tolerable range. The test results are shown in Fig. 10(b), where it may be seen that the in-



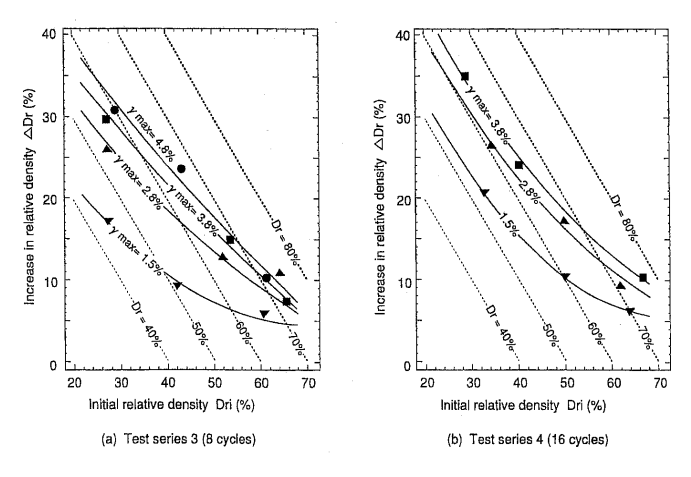


Fig. 10. Summary of undrained shear test results: (a) Test series 3 (8 cycles), (b) Test series 4 (16 cycles)

crement ΔD_r became somewhat greater as compared with the case of the 8 cycle load application shown in Fig. 10(a). All the tests shown in Fig. 10 were conducted at an effective consolidation pressure of 100 kPa, with the actual stress conditions encountered in practice in mind. Therefore, as the initial consolidation pressure becomes larger than that used in this study, the soil density increase may become less than expected in the diagram presented herein.

Evaluation of the Maximum Shear Strain

If the above experimental results are to be compared with the field performance represented by an in-situ parameter such as SPT N values, the amount of the deviatoric strain γ_{max} that occurs in the field needs to be assessed. The model of cylindrical cavity expansion may be used for this purpose in which a cylindrical cavity is postulated to expand from zero radius in an infinite, incompressible, isotropic and homogeneous media. Suppose a cylindrical cavity expands from zero to a radius R and the soil particle at an initial position of r_o is displaced to a position of r, the following equation holds true,

$$r^2\pi - R^2\pi = r_o^2\pi. \tag{5}$$

The radial strain ε_r , with respect to the displaced position is defined as follows;

$$\varepsilon_r = \frac{\partial (r - r_o)}{\partial r} = 1 - \frac{\partial r_o}{\partial r} = -\frac{r - r_o}{r_o}, \tag{6}$$

where r- r_o is the radial displacement. The replacement ratio used commonly in practice is defined as;

$$a_s(\%) = 100 \times \pi r_p^2 / L^2,$$
 (7)

where r_p is the radius of the sand pile, and L is the distance between the adjacent piles. On the other hand, by assuming constant-volume deformation due to undrained nature of pile installation, the relations, $\varepsilon_r + \varepsilon_\theta = 0$, $\varepsilon_z = 0$ and $\varepsilon_{r\theta} = 0$, are required for cylindrical cavity expansion. In this case, the deviatoric strain γ defined for the hollow cylindrical soil specimens can be expressed with respect to ε_r defined for the model of cylin-

drical cavity expansion as $\gamma = 2/\sqrt{3} \varepsilon_r$ ($= 1.155 \varepsilon_r$). However, the constant-volume deformation assuming the equation of $\varepsilon_r + \varepsilon_\theta + \varepsilon_z = 0$ might be more realistic to account for the heave of the ground surface that may occur during the course of sand pile installation. In this case, for instance, the assumption of $\varepsilon_r + \varepsilon_\theta + \varepsilon_z = 0$ and $\varepsilon_z = -1/10\varepsilon_r$ is reduced to $\gamma = 1.102\varepsilon_r$. In what follows, however, due to the difficulty in properly evaluating the magnitude of the ground surface heave, the condition of $\varepsilon_r + \varepsilon_\theta = 0$ and $\varepsilon_z = 0$ is assumed. Furthermore, based on the observation of the test results in which, in the course of the undrained torsional tests simulating penetration of one sand pile, the deviatoric strain γ is increased up to $\gamma_{\rm max}$ during the loading and is reduced during unloading down almost to half the magnitude of γ_{max} , it can be assumed that due to the simulation of penetration of four sand piles, the residual strain of $2\gamma_{max}$ is induced. Therefore, it is reasonable to assume that the shear strain γ defined in the above equation can be replaced by $2\gamma_{\text{max}}$. It should also be noted here that the strain $\varepsilon_{z\theta}$ is one of the major components of strain induced in hollow cylindrical torsional shear tests, whereas ε_r and ε_{θ} are the major components of strain for the model of cylindrical cavity expansion. Therefore, the shearing modes induced in the above two conditions may be somewhat different, where the deformation of the soil specimens occurs in a manner more similar to simple shear in the hollow cylindrical torsional shear tests, and the cavity expansion theory imposes the deformation in a manner similar to biaxial compression. Suppose the shear strains induced by the above two deformation modes are in effect identical, and the effect of $\varepsilon_{z\theta}$ is assumed to be small, by combining Eqs. (5), (6) and (7) and replacing R to r_p and r_o to $L/\sqrt{2}$ due to the geometrical requirement of a sand pile configuration, the deviatoric strain γ_{max} can be converted to the replacement ratio a_s .

It is known that the relative density D_r (%) of sand can be converted to the SPT N_1 value by an empirical equation, (Skempton, 1986; Ishihara, 1993),

$$N = (a + b\sigma'_v) \left(\frac{D_r}{100}\right)^2, \quad N_1 = (a + b) \left(\frac{D_r}{100}\right)^2,$$
 (8)

where a and b are constants which depend mainly on the grain size and σ'_v denotes the effective overburden pressure in kgf/cm². N_1 implies the N-value of a soil deposit undergoing an overburden pressure of $\sigma'_v = 1 \text{ kgf/cm}^2$. According to the data compiled by Ishihara (1993), the constant a+b may take a value of 70 for clean sand. Therefore, a diagram such as Fig. 10(b) can be converted to a diagram in which changes in SPT N_1 values before and after densification are expressed in terms of γ_{max} or more practically in terms of the replacement ratio a_s . As described later, this type of diagram thus obtained may be able to provide a basis for the assessment of volume changes of soils due to static sand pile driving and installation.

Case Studies on Soil Densification

The experimental results described above showed that

changes in the state of stress due to static sand pile penetration are capable of significantly densifying loose to medium dense soils to a degree great enough to meet the design requirement. The experimental evidence mentioned above would provide a logical basis for the assessment of the degree of soil densification due to statically conducted sand pile penetration.

In order to provide field evidence of effectiveness in such sand pile penetration, case studies were made on actual soil densification projects carried out at three sites, Site A, Site B, and Site C. Figure 11 shows plan views and spacing of static sand pile installation and distribution of SPT N values with depth before and after the sand pile installation, at respective sites. In this diagram, a_s denotes a replacement ratio, and F_c denotes a fines content. Sand piles with a diameter of 70 cm were installed at all the three sites. However, the spacing of the sand piles was different at each site, so different replacement ratios a_s were adopted at the three sites, ranging from about 10 to 23%. Shown in Fig. 12 are the SPT N_1 values before and after densification obtained at the three sites, and a group of curves proposed for evaluating the increase in SPT N_1 values due to static sand pile installation. These curves are those interpolated from the data through conversion of the laboratory test results mentioned above. The SPT N_1 values plotted in this diagram are those measured at depths from 3 to 12 metres below the ground level at each site, where fines content F_c was greater than 20%. Although there are scatters in the in-situ SPT N_1 values, this chart may be used to provide preliminary estimates to the increase in SPT N_1 values due to static sand pile installation.

The data presented in Fig. 12 are those for replacement ratios a_s greater than about 10%; the charts for evaluating increases in SPT N_1 values at replacement ratios lower than 10% are not shown because of a lack of relevant data. To extrapolate the evaluation charts for lower replacement ratios, the in situ SPT N values at other sites were collected and compiled. These included cases of

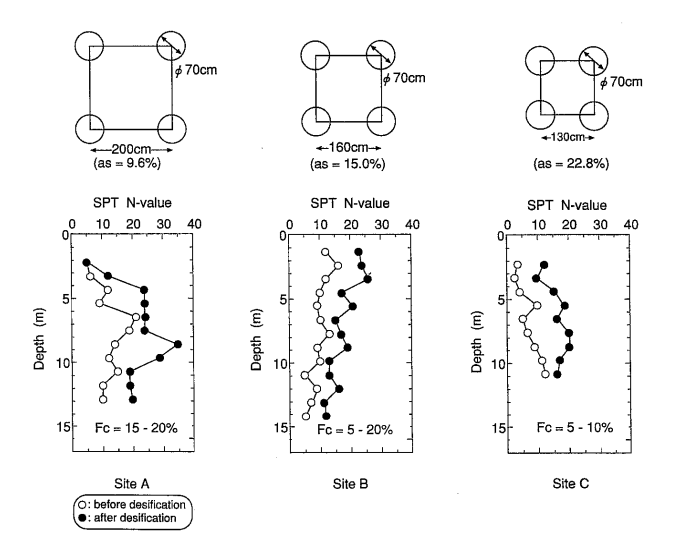


Fig. 11. Soil profiles for case studies

compaction by means of sand drain (SD), rod compaction (RC) and sand compaction pile (SCP) reported by Tsuboi et al. (1996). Needless to say, the installation procedures of those compaction piles are different from the static sand pile installation method examined here. However, the results of the compilation are displayed in Fig. 13. In these data, the SPT N_1 values were calculated by the equation of $N_1=N/1.7$, $(N_1=N/(\sigma_v+0.7)$ at $\sigma_v=1$ kgf/cm²), (Meyerhof, 1957). It can be seen that the curves for $a_s=2\%$ and 6% show a satisfactory degree of

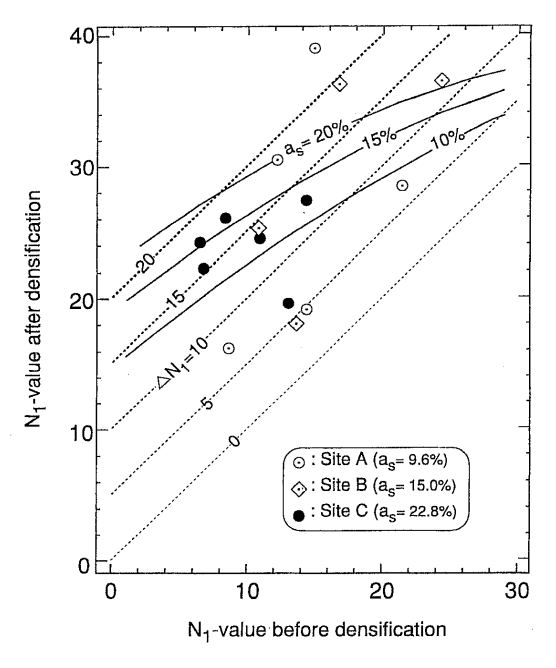


Fig. 12. SPT N_1 -values before and after densification at high replacement ratios

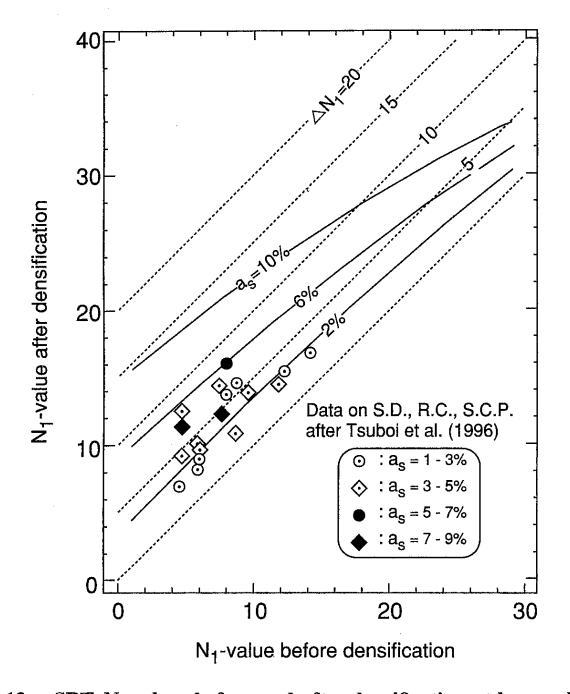


Fig. 13. SPT N_1 -values before and after densification at low replacement ratios

18

TSUKAMOTO ET AL.

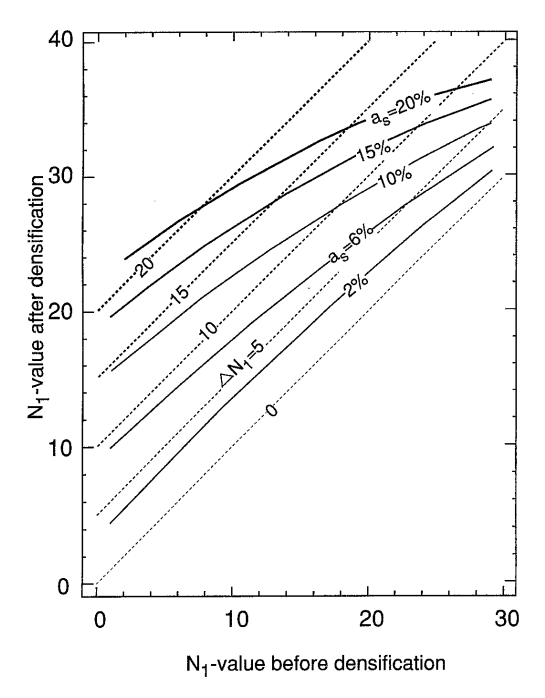


Fig. 14. Diagram for the evaluation of SPT N_1 -value increase

agreement with the data from the two sources. By combining the curves in Figs. 12 and 13, a chart for evaluating increases of the SPT N_1 value can be produced as shown in Fig. 14.

There may be several factors responsible for causing the difference between the experimental results and the field data. First of all, volume change characteristics studied here refer only to those for fine sand with little fines, whereas real soils in the fields may contain more fines. These features should be taken careful note for evaluating densification characteristics of in-situ soil deposits.

CONCLUSIONS

Large-scale hollow cylindrical torsional shear tests were conducted on fine sand, to study soil densification characteristics due to static sand pile driving and installation, such as a sand compaction pile used for improving loose deposits of sandy soils. Special reference was made to drained and undrained responses and subsequent volume changes of sand. Field stress paths were first calculated with an assumption of the theory of elasticity. Drained shear tests were first conducted by reproducing the above-calculated field stress path in the laboratory specimens. The results of these tests disclosed that densification under drained conditions was not great enough to generate the volume decrease corresponding to that likely to occur in the field. Undrained shear tests were also conducted on several simplified stress paths. In undrained tests, the influence of shear strains of the order of $\gamma_{\text{max}} = 3\%$ imposed on the soil specimens was found to be large enough to produce significant densification, which can account for actual situations occurring in the field during installation of sand piles. The experimental results of the test series described herein are considered to be able to provide a basis for the preliminary assessment of soil densification due to static sand pile penetration, and as such a diagram for evaluating densification effects in terms of the SPT N_1 value was created and is presented in this paper. Case studies were also carried out on soil densification due to static sand pile installation at three sites, and the comparison was made with the proposed evaluation diagram.

ACKNOWLEDGEMENTS

The first author would like to acknowledge the financial assistance provided by Maeda Memorial Engineering Foundation. The authors also express their sincere thanks to Mr. T. Inami for his cooperation in carrying out the experiments reported in this paper.

NOTATION

- a_s replacement ratio
- (a, 0) location of unit force
 - b coefficient of intermediate principal stress
 - d unit depth
- (d, R) location of point P
 - e void ratio
- e_{max} , e_{min} maximum and minimum void ratios
 - e_N void ratio observed after Nth cycle
 - e_0 initial void ratio
 - (p, q) mean and deviator stresses on the hollow cylindrical specimen
- (\bar{p}, \bar{q}) two-dimensional mean and deviator stresses on the hollow cylindrical specimen
- (\bar{p}_s, \bar{q}_s) two-dimensional mean stress and deviator stress induced at point P
 - current radial position for the model of cylindrical cavity expansion
 - r_o initial radial position for the model of cylindrical cavity expansion
 - r_p radius of sand piles
- r_0 , r_1 , r_2 parameters for the calculation of the field stress path (Appendix)
 - excess pore water pressure
 - vertical displacement
 - (z, r) polar coordinates for axi-symmetric pile penetration
 - z₁ parameter for the calculation of the field stress path (Appendix)
- A, B, C, D parameters for the calculation of the field stress path (Appendix)
 - D_r relative density
 - D_{ri} initial relative density
 - D₅₀ mean diameter
 - F_c fines content
 - G shear modulus
 - G_s specific gravity
 - \vec{L} distance between adjacent two piles
 - N SPT N values
 - N_1 SPT N_1 values
 - P_i inner cell pressure
 - P_o outer cell pressure
 - R radius for the model of cylindrical cavity expansion
 - T torque
 - U_c uniformity coefficient
 - V vertical force
 - ΔV_i inner cell volume change

 ΔV_s specimen volume change

 V_{si} initial specimen volume

 α angle of principal stress direction

 α , β parameters for the calculation of the field stress path (Appendix)

. volumetric strain

 ε_r radial strain for the model of cylindrical cavity expansion

 $(\varepsilon_z, \varepsilon_r, \varepsilon_\theta \text{ and } \varepsilon_{z\theta})$ strains induced on the hollow cylindrical specimen $(\varepsilon_1, \varepsilon_2, \text{ and } \varepsilon_3)$ principal strains induced on the hollow cylindrical specimen

y deviatoric strain

 γ_a accumulated deviatoric strain

 $\gamma_{\rm max}$ maximum deviatoric strain

ν Poisson's ratio

 θ rotation angle of the hollow cylindrical specimen

 σ_{ν} overburden pressure

 $(\sigma_r, \sigma_z, \sigma_{rz}, \sigma_\theta)$ stresses induced at point P

 $(\sigma_z, \, \sigma_r, \, \sigma_\theta \, \text{and} \,$

 $\sigma_{z\theta}$) stresses induced on the hollow cylindrical specimen $\sigma_1, \sigma_2, \sigma_3$) principal stresses induced on the hollow cylindrical specimen

N.B. All the above stress components with "'" introduce the corresponding effective stress components.

REFERENCES

- Fudo Construction Co., Ltd. (1996): "Internal report on field measurement of static sand pile installation at several project sites," (in Japanese).
- Ishihara, K. (1993): "Liquefaction and flow failure during earthquakes," Géotechnique, Vol. 43, No. 3, pp. 351-415.
- Japanese Society of Soil Mechanics and Foundation Engineering (1978): "From in-situ survey and design to installation of soil improvement against liquefaction," (in Japanese).
- 4) Kusano, K. (1983): "Some thoughts on practical aspects and problems of deep soil improvement—practice and problems of sand compaction pile method (3)—," Tsuchi-to-Kiso, Japanese Society of SMFE, Vol. 31, No. 4, pp. 79-86 (in Japanese).
- 5) Meyerhof, G. G. (1957): "Discussion on research on determining the density of sands by spoon penetration testing," Proc. 4th Int. Conf. on SMFE, Vol. 3, pp. 110.
- Mindlin, R. D. (1936): "Force at a point in the interior of a semiinfinite solid," Physics, Vol. 7, pp. 195-202.
- Mizuno, Y., Suematsu, N. and Okuyama, K. (1987): "Design method of sand compaction pile for sandy soils containing fines," Tsuchi-to-Kiso, Japanese Society of SMFE, Vol. 35, No. 5, pp. 21– 26 (in Japanese).
- 8) Mogami, T. (1957): "Numerical tables for calculation of stress components induced in a semi infinite elastic solid when a force is applied at a point in the interior of the body," Kajima Construction Technical Research Institute.
- Port and Harbour Research Institute, Ministry of Transport, Japan (eds.) (1997): Handbook on Liquefaction Remediation of Reclaimed Land, A. A. Balkema.
- 10) Skempton, A. W. (1986): "Standard penetration test procedures and the effects in sands of overburden pressure, relative density, particle size, aging and overconsolidation," Géotechnique, Vol. 36, No. 3, pp. 425-447.
- 11) Symes, M. J. P. R., Gens, A. and Hight, D. W. (1984): "Undrained anisotropy and principal stress rotation in saturated sand," Géotechnique, Vol. 34, No. 1, pp. 11-27.
- 12) Tsuboi, H., Takahashi, Y., Harada, K. and Nitao, H. (1996): "Comparing remedial measure against soil liquefaction on reclaimed lands," Tsuchi-to-Kiso, The Japanese Geotechnical Society, Vol. 44, No. 2, pp. 67-69 (in Japanese).

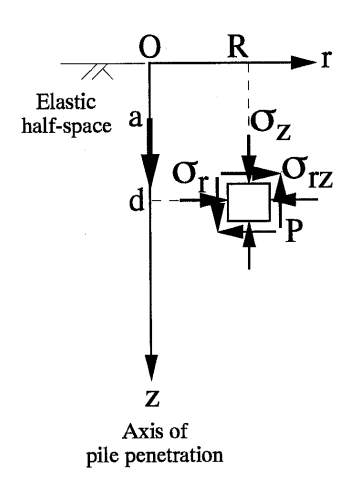


Fig. A1. Calculation of field stress path due to pile driving

APPENDIX

Calculation Procedure for Field Stress Path

The calculation procedure for the field stress path due to sand pile driving is described herein. The solution of the problem of a single force applied in the interior of an elastic half space (semi-infinite solid) in the reference by Mogami (1957) is utilized. Figure A1 shows the polar coordinates (r, z), in which an elastic half space occupies the region of z>0, and a soil element P is located at (R, d), (d=1, unit depth), and a unit vertical force acts at (0, a). The stress components $(\sigma_r, \sigma_z, \sigma_{rz}, \sigma_\theta)$ at point P can be calculated by the expressions given by Mogami (1957).

In what follows, compressive stresses are taken as positive. Suppose the unit vertical force advances along the z-axis from the origin O to some depth many times greater than the depth of the soil element P, the stress state at point P changes with the position of the unit vertical force. Accordingly, the field stress path experienced by the soil element P can be obtained. Herein, it is assumed that the depth of the unit vertical force a is $a=\alpha d$ $(0<\alpha \le 5, d=1$: unit depth), and the soil element P is located at (R, d), where $R=\beta d$. Poisson's ratio v of 0.5 is assumed, which corresponds to an undrained condition from a geotechnical viewpoint. The stress components induced at point P can be written as follows,

$$\sigma_r = \frac{2}{\alpha^2} A$$
, $\sigma_z = -\frac{2}{\alpha^2} B$, $\sigma_{rz} = -\frac{2}{\alpha^2} C$, $\sigma_\theta = \frac{2}{\alpha^2} D$, (A1)

where A, B, C and D are defined as follows,

$$A = \frac{1}{8\pi} \left\{ \frac{3r_o^2(z_1 - 1)}{r_1^5} + \frac{6(z_1 + 1)}{r_2^5} + \frac{30r_o^2z_1(z_1 + 1)}{r_2^7} + \frac{3r_o^2(z_1 - 1)}{r_2^5} \right\},$$

$$B = -\frac{1}{8\pi} \left\{ \frac{3(z_1 - 1)^3}{r_1^5} + \frac{3z_1(z_1 + 1)^2}{r_2^5} + \frac{3z_1(z_1 + 1)^2}{r_2^$$

20

TSUKAMOTO ET AL.

$$-\frac{3(z_1+1)(5z_1-1)}{r_2^5} + \frac{30z_1(z_1+1)^3}{r_2^7} \bigg\},$$

$$C = -\frac{r_o}{8\pi} \left\{ \frac{3(z_1-1)^2}{r_1^5} + \frac{3z_1(z_1+1)}{r_2^5} - \frac{3(3z_1+1)}{r_2^5} + \frac{30z_1(z_1+1)^2}{r_2^7} \right\},$$

$$D = \frac{3}{4\pi} \frac{z_1+1}{r_2^5},$$

and
$$r_{o} = \frac{R}{a} = \frac{\beta d}{\alpha d} = \frac{\beta}{\alpha}, \quad z_{1} = \frac{d}{a} = \frac{d}{\alpha d} = \frac{1}{\alpha},$$

$$r_{1} = \sqrt{r_{o}^{2} + (z_{1} - 1)^{2}} = \sqrt{(\beta/\alpha)^{2} + \left(\frac{1}{\alpha} - 1\right)^{2}},$$

$$r_{2} = \sqrt{r_{o}^{2} + (z_{1} + 1)^{2}} = \sqrt{(\beta/d)^{2} + \left(\frac{1}{\alpha} + 1\right)^{2}}.$$
(A3)